Journal of Computational Mathematics
Vol.xx, No.x, 2025, 1–25.

http://www.global-sci.org/jcm
doi:10.4208/jcm.2502-m2024-0015

INVARIANT REGION PRESERVING RECONSTRUCTION AND ENHANCED STABILITY OF THE CENTRAL SCHEME IN TWO DIMENSIONS*

Ruifang Yan
School of Mathematics and Statistics, Wuhan University, Wuhan 430072, China;
Hubei Key Laboratory of Computational Science, Wuhan University, Wuhan 430072, China;
Department of Mathematics and Shenzhen International Center for Mathematics,
Southern University of Science and Technology, Shenzhen 518055, China
Wei Tong
School of Mathematics and Statistics, Wuhan University, Wuhan 430072, China;
Hubei Key Laboratory of Computational Science, Wuhan University, Wuhan 430072, China;
School of Mathematics and Statistics, Hubei Engineering University, Xiaogan 432000, China
Guoxian Chen[1)]
School of Mathematics and Statistics, Wuhan University, Wuhan 430072, China;
Hubei Key Laboratory of Computational Science, Wuhan University, Wuhan 430072, China
Email: gxchen.math@whu.edu.cn

Abstract

In this paper, our focus is on examining the robustness of the central scheme in two dimensions. Although stability analyses are available in the literature for the scheme's solution of scalar conservation laws, the associated Courant-Friedrichs-Lewy (CFL) number is often notably small, occasionally degenerating to zero. This challenge is traced back to the initial data reconstruction. The interface value limiter used in the reconstruction proves insufficient to maintain the invariant region of the updated solutions. To overcome this limitation, we introduce the vertex value limiter, resulting in a more suitable CFL number that is half of the one-dimensional value. We present a unified analysis of stability applicable to both types of limiters. This enhanced stability condition enables the utilization of larger time steps, offering improved resolution to the solution and ensuring faster simulations. Our analysis extends to general conservation laws, encompassing scalar problems and nonlinear systems. We support our findings with numerical examples, validating our claims and showcasing the robustness of the enhanced scheme.

Mathematics subject classification: 76M12, 35L65.
Key words: Hyperbolic conservation laws, Central scheme, Invariant-region-preserving principle, MUSCL-type interpolant, Interface value limiter, Vertex value limiter.

1. Introduction

This paper aims to enhance the central scheme (CS) in two dimensions (2D) used for solving hyperbolic conservation laws, which commonly describe numerous problems in applied mathematics, physics, and engineering sciences. The admissible state Ω of the solution vector $\mathbf{u}(\mathbf{x}, t)$ forms an invariant set meaning that it is convex and

$$\mathbf{u}(\mathbf{x}, t = 0) \in \Omega \implies \mathbf{u}(\mathbf{x}, t \geq 0) \in \Omega, \quad \forall\, \mathbf{x} = (x, y) \in \mathbb{R}. \tag{1.1}$$

* Received January 14, 2024 / Revised version received July 18, 2024 / Accepted February 17, 2025 / Published online April 14, 2025 /
1) Corresponding author

We refer to the above property as the invariant-region-preserving (IRP) principle. For scalar nonlinear conservation laws, the concept of the IRP principle is closely connected with the minimum-maximum-preserving (MMP) principle. In the case of nonlinear Euler equations, it is substituted by the positivity-preserving (PP) principle. The achievement of satisfying the IRP principle has become a key topic in recent literature [3,4,7,9,12,13,25,32,37], among other references.

The CS scheme stands out as a versatile tool capable of addressing a wide array of diverse problems, owing to its avoidance of Riemann solvers and characteristic decomposition [10,11,24,26]. In 1990, Nessyahu and Tadmor [24] introduced the NT scheme (one dimensional central scheme), a natural second-order extension of the first-order Lax-Friedrichs method. This method utilizes MUSCL-type interpolants to alleviate excessive numerical viscosity. The authors provided a detailed total variation diminishing (TVD) stability analysis for this approach, specifically focusing on resolving one-dimensional (1D) scalar conservation laws. When tackling more intricate challenges, such as nonlinear Euler equations and shallow water equations, among others [14,18,28], a specific linearization step is incorporated. To validate the updated solution for general nonlinear systems, we adjusted the preliminary reconstructed derivative of the solution using an extended IRP limiter [33,34]. In the predictor step, the flux derivative is constructed through the central difference method using interpolated interface values. The IRP condition for the 1D solver has been updated and uniformly proven through a forward-backward decomposition method.

Several extensions to the scheme have been developed, including two-dimensional extensions (CS2D) [11], the unstaggered version [10], various configurations of staggered cells [1, 2], the variant involving overlapping cells [19, 22, 23], and the central upwind method [15, 16], among others.

This paper specifically addresses the robustness of the CS2D scheme [10, 11, 29, 30]. To mitigate oscillations, Jiang and Tadmor [11] employed the generalized minmod limiter (3.4) with a parameter θ ranging between 1 and 2. This limiter is applied to reconstruct the x- and y-derivatives, as detailed in (3.3), ensuring the boundedness of interpolated interface values. It is widely acknowledged that the 2D upwind-type scheme, with such initial data reconstruction, allows for a Courant-Friedrichs-Lewy number that is half of the 1D case, as the scheme is equivalent to an average of two 1D solvers. However, the MMP stable condition, as stated in [10, 11], indicates that the 2D CFL number is significantly small and even reaches zero when the parameter $\theta = 2$ (3.10). Lie and Noelle [20] replaced the midpoint method with the trapezoidal method to compute the time integral of the numerical flux, enhancing the resolution of certain waves. However, this adjustment did not improve the CFL number. The stability conditions mandate small time steps, leading to considerable numerical dissipation, solution smearing [16, 21–23], and, ultimately, much longer simulation times.

In contrast to the upwind scheme, the crucial step of the CS scheme involves calculating the flux within the cell center, where the solution remains continuous. This differs from the upwind scheme, where the flux is traditionally computed along the cell boundaries, and the solution is assumed to be discontinuous. The evolution of the projected solution takes place in the dual cells. The CFL condition plays a crucial role in regulating the time step, ensuring that the accumulated flux over this time interval does not surpass the total mass of the dual cells.

Our key observation centers on the potential bias between the projection step and the limiting process during initial data reconstruction. This bias can lead to the projected solution being disproportionately small compared to the flux, resulting in excessively small time steps.

The conventional dimensional splitting reconstruction method with an interface value limiter (IVL) exemplifies such an approach. To mitigate this, we transition to the vertex value limiter (VVL), which differs slightly from the IVL method but guarantees favorable properties of the projected solution. Moreover, it eliminates the bias present in the IVL process. It is noteworthy that these two types of limiters can be uniformly described, facilitating a comprehensive analysis of stability.

The paper is organized as follows. Firstly, an overview of the general procedure of the CS2D scheme is presented in Section 2. Section 3 delves into the limiting process, where we revisit the conventional IVL method and derive a VVL method. This section includes an example that compares these two types of limiters. Section 4 offers a unified analysis based on the forward-backward decomposition technique. In Section 5, a series of numerical tests are provided to validate the analysis and showcase the robustness of the proposed scheme. The paper concludes with a summary in Section 6.

2. The Review of Central Scheme

In this section, we will go over the general procedure of the CS scheme for solving 2D hyperbolic conservation laws

$$\mathbf{u}_t + \mathbf{f}(\mathbf{u})_x + \mathbf{g}(\mathbf{u})_y = 0 \tag{2.1}$$

with appropriate initial and boundary conditions. Let us denote the conservative vector as $\mathbf{u} = (u_1, u_2, \cdots, u_p)$, and represent the flux functions as $\mathbf{f} = (f_1, f_2, \cdots, f_p)$ and $\mathbf{g} = (g_1, g_2, \cdots, g_p)$. It is important to note that the equations mentioned earlier, denoted as (2.1), are often nonlinear in nature.

Given a uniform grid $x_\alpha := \alpha\Delta x$ and $y_\beta := \beta\Delta y$ covering the computational domain, we define the grid point $\mathbf{x}_{\alpha,\beta} = (x_\alpha, y_\beta)$ and the cell $C_{\alpha,\beta}$ centered around $\mathbf{x}_{\alpha,\beta}$ as follows:

$$C_{\alpha,\beta} := \left[x_{\alpha-\frac{1}{2}}, x_{\alpha+\frac{1}{2}}\right] \times \left[y_{\beta-\frac{1}{2}}, y_{\beta+\frac{1}{2}}\right]. \tag{2.2}$$

We refer to the primal cell as $C_{i,j}$ and the dual cell as $C_{i+1/2,\,j+1/2}$ $(i \in \mathbb{Z}, j \in \mathbb{Z})$ (Fig. 2.1).

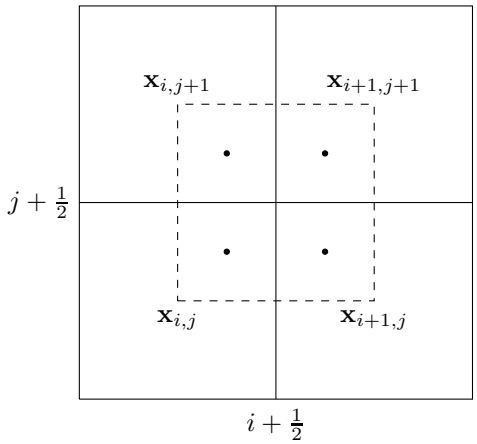

Fig. 2.1. A dual cell $C_{i+1/2,\,j+1/2}$ (bounded by dashed lines). Its four vertexes are the centers of the surrounding primal cells. Projection points: •.

The cell-average is defined as

$$\mathbf{u}_{\alpha,\beta}(t) := \frac{1}{\Delta x \Delta y} \iint_{C_{\alpha,\beta}} \mathbf{u}(\mathbf{x}, t) d\mathbf{x}. \tag{2.3}$$

By employing an initial data reconstruction method, we obtain the piecewise linear approximation of the solution

$$\mathcal{L}_{\alpha,\beta}(\mathbf{x}) := \mathbf{u}_{\alpha,\beta} + \Delta_x \mathbf{u}_{\alpha,\beta} \frac{x - x_\alpha}{\Delta x} + \Delta_y \mathbf{u}_{\alpha,\beta} \frac{y - y_\beta}{\Delta y}, \quad \forall\, \mathbf{x} \in C_{\alpha,\beta}, \tag{2.4}$$

where $\Delta_x \mathbf{u}_{\alpha,\beta}/\Delta x$ and $\Delta_y \mathbf{u}_{\alpha,\beta}/\Delta y$ represent the discrete derivatives of the solution.

The second-order unstaggered CS scheme [10] consists of three steps: forward projection, evolution, and backward projection.

Projections. Prior to the evolution of the solutions, the values $\mathbf{u}^n_{i,j}$ need to be projected onto the dual cells $C_{i+1/2,j+1/2}$. After the evolution, the updated solutions $\mathbf{u}^{n+1}_{i+1/2,\,j+1/2}$ are projected back onto the primal cells $C_{i,j}$, resulting in an unstaggered version of the scheme.

We consider the projections onto the cell $C_{\alpha+1/2,\,\beta+1/2}$ in the forward projection step (with $(\alpha,\beta) = (i,j)$) or in the backward projection step (with $(\alpha,\beta) = (i+1/2,\, j+1/2)$). There are four surrounding cells that have nonempty intersections with $C_{\alpha+1/2,\,\beta+1/2}$. These surrounding cells are $C_{\alpha,\beta}, C_{\alpha+1,\beta}, C_{\alpha+1,\beta+1}$ and $C_{\alpha,\beta+1}$. The cell-average (2.3) on $C_{\alpha+1/2,\,\beta+1/2}$ can be precisely calculated as follows:

$$\mathbf{u}_{\alpha+\frac{1}{2},\,\beta+\frac{1}{2}} := \frac{1}{4} \sum_{i'=0,1;\, j'=0,1} \mathcal{L}_{\alpha+i',\beta+j'}\big(\mathbf{x}_{\alpha+\frac{1}{4}+\frac{i'}{2},\beta+\frac{1}{4}+\frac{j'}{2}}\big), \tag{2.5}$$

using the interpolated solutions by (2.4) at the center points of the line segments connecting the cell center and the centers of four surrounding cells

$$\mathbf{x}_{\alpha+\frac{i'}{4},\beta+\frac{i'}{4}} = \frac{1}{2}\big(\mathbf{x}_{\alpha,\beta} + \mathbf{x}_{\alpha+\frac{i'}{2},\beta+\frac{j'}{2}}\big), \quad i' = \pm 1, \quad j = \pm 1, \tag{2.6}$$

which is referred to as "projection points". Fig. 2.1 provides a visual representation of these cells and projection points.

Evolution. The solution after the forward projection is evolved in a two-step method:

- Predictor step: Estimate the solution at the half time step in the primal cells

$$\begin{cases} \mathbf{u}^{n+\frac{1}{2}}_{i,j} := \mathbf{u}^n_{i,j} + \dfrac{\Delta t}{2} \mathbf{R}^n_{i,j}, \\ \mathbf{R}^n_{i,j} := -\dfrac{\Delta_x \mathbf{f}^n_{i,j}}{\Delta x} - \dfrac{\Delta_y \mathbf{g}^n_{i,j}}{\Delta y}, \end{cases} \tag{2.7}$$

  where $\Delta_x \mathbf{f}^n_{i,j}/\Delta x$ and $\Delta_y \mathbf{g}^n_{i,j}/\Delta y$ represent the inner approximations of the derivatives of the flux in the cell $C_{i,j}$. In the cited references [11, 24, 30], these flux derivatives are approximated either directly by reconstructing fluxes or by using derivatives of solutions. Specifically, $\Delta_x \mathbf{f}_{i,j}$ is approximated as $\mathbf{f}_{\mathbf{u}}(\mathbf{u}_{i,j})\Delta_x \mathbf{u}_{i,j}$, and $\Delta_y \mathbf{g}_{i,j}$ is approximated as $\mathbf{g}_{\mathbf{u}}(\mathbf{u}_{i,j})\Delta_y \mathbf{u}_{i,j}$. The properties of TVD in one dimension and MMP in two dimensions have been proven for scalar conservation laws. However, it is important to note that

these stability results are not applicable to nonlinear systems such as the Euler equations and shallow water equations. Nonlinear systems introduce additional complexities, and the stability and accuracy of numerical methods for such systems need to be carefully examined and established.

To unify the stabilities, we follow [33, 34] and approximate the flux derivatives as

$$\begin{cases} \Delta_x \mathbf{f}_{i,j} := \mathbf{f}\big(\mathcal{L}_{i,j}\big(\mathbf{x}_{i+\frac{1}{2},j}\big)\big) - \mathbf{f}\big(\mathcal{L}_{i,j}\big(\mathbf{x}_{i-\frac{1}{2},j}\big)\big), \\ \Delta_y \mathbf{g}_{i,j} := \mathbf{g}\big(\mathcal{L}_{i,j}\big(\mathbf{x}_{i,j+\frac{1}{2}}\big)\big) - \mathbf{g}\big(\mathcal{L}_{i,j}\big(\mathbf{x}_{i,j-\frac{1}{2}}\big)\big), \end{cases} \tag{2.8}$$

using the interpolated solutions by the reconstruction (2.4).

- Corrector step: Update the projected solution $\mathbf{u}^n_{i+1/2,\,j+1/2}$ in the dual cell $C_{i+1/2,\,j+1/2}$

$$\begin{cases} \mathbf{u}^{n+1}_{i+\frac{1}{2},j+\frac{1}{2}} := \mathbf{u}^{n}_{i+\frac{1}{2},j+\frac{1}{2}} + \Delta t \mathbf{R}^{n+\frac{1}{2}}_{i+\frac{1}{2},j+\frac{1}{2}}, \\ \mathbf{R}^{n+\frac{1}{2}}_{i+\frac{1}{2},j+\frac{1}{2}} := -\dfrac{1}{\Delta x}\left(\mathbf{f}^{n+\frac{1}{2}}_{i+1,j+\frac{1}{2}} - \mathbf{f}^{n+\frac{1}{2}}_{i,j+\frac{1}{2}}\right) - \dfrac{1}{\Delta y}\left(\mathbf{g}^{n+\frac{1}{2}}_{i+\frac{1}{2},j+1} - \mathbf{g}^{n+\frac{1}{2}}_{i+\frac{1}{2},j}\right) \end{cases} \tag{2.9}$$

with

$$\begin{aligned} \mathbf{f}^{n+\frac{1}{2}}_{i,j+\frac{1}{2}} &:= \frac{1}{2}\left(\mathbf{f}\left(\mathbf{u}^{n+\frac{1}{2}}_{i,j}\right) + \mathbf{f}\left(\mathbf{u}^{n+\frac{1}{2}}_{i,j+1}\right)\right), \\ \mathbf{g}^{n+\frac{1}{2}}_{i+\frac{1}{2},j} &:= \frac{1}{2}\left(\mathbf{g}\left(\mathbf{u}^{n+\frac{1}{2}}_{i,j}\right) + \mathbf{g}\left(\mathbf{u}^{n+\frac{1}{2}}_{i+1,j}\right)\right), \end{aligned} \tag{2.10}$$

using the predicted solutions.

To implement the aforementioned algorithm, it is required that the interface values, evaluated at midpoints, conform to the invariant region

$$\mathcal{L}_{\alpha,\beta}(\mathbf{x}) \in \Omega, \quad \forall\, \mathbf{x} \in \mathbb{I}_{\alpha,\beta} := \left\{\mathbf{x}_{\alpha-\frac{1}{2},\beta}, \mathbf{x}_{\alpha+\frac{1}{2},\beta}, \mathbf{x}_{\alpha,\beta-\frac{1}{2}}, \mathbf{x}_{\alpha,\beta+\frac{1}{2}}\right\}. \tag{2.11}$$

Alternatively, this condition can be expressed as

$$\mathbf{u}_{\alpha,\beta} \pm \frac{1}{2}\Delta \mathbf{u}_{\alpha,\beta} \in \Omega, \quad \Delta = \Delta_x \ \text{ or } \ \Delta_y. \tag{2.12}$$

Owing to the linearity of the function $\mathcal{L}_{\alpha,\beta}(\mathbf{x})$ and the convex nature of the invariant region Ω, it can be inferred that the value of the projection point, situated at the center of the interval connecting two interface midpoints, also falls within the invariant region. It is worth mentioning that the condition (2.11) or (2.12) is invariably used for the second-order upwind type MUSCL scheme which employs these quantities to determine the numerical fluxes.

3. IRP Initial Data Reconstruction

In this section, we will explore the limiting process. This process is generally independent of the evolution step, and it significantly impacts the CFL condition for stability. By analyzing the shortcomings of the conventional interface value limiter, we derive a vertex value limiter, which aids in relaxing the stability condition.

3.1. Examination of the interface value limiter

To streamline our discussion, let us take the scalar hyperbolic conservation law as our model

$$u_t + f(u)_x + g(u)_y = 0, \quad u(x, y, t = 0) = u_0(x, y). \tag{3.1}$$

In this scenario, the invariant region is an interval

$$\Omega = \Big[\min_{x,y} u_0(x, y),\ \max_{x,y} u_0(x, y) \Big]. \tag{3.2}$$

In this case, the IRP property transforms into the minimum-maximum-preserving property.

In order to achieve a second-order oscillation-free approximation, it is crucial to construct the piecewise gradient of the solutions using the cell averages. In the study [11], van Leer's one-parameter family of the minmod method, which is based on one-dimensional flow physics, is employed

$$\begin{cases} \Delta_x u_{\alpha,\beta} = \mathrm{MM}_\theta(u_{\alpha-1,\beta}, u_{\alpha,\beta}, u_{\alpha+1,\beta}), \\ \Delta_y u_{\alpha,\beta} = \mathrm{MM}_\theta(u_{\alpha,\beta-1}, u_{\alpha,\beta}, u_{\alpha,\beta+1}) \end{cases} \tag{3.3}$$

with

$$\mathrm{MM}_\theta(q_1, q_2, q_3) := \mathrm{minmod}\bigg(\theta(q_2 - q_1), \frac{q_3 - q_1}{2}, \theta(q_3 - q_2) \bigg), \tag{3.4}$$

where

$$\mathrm{minmod}(z_1, z_2, z_3) := \min_j\{\max(z_j, 0)\} + \max_j\{\min(z_j, 0)\}.$$

The parameter $\theta \in [1, 2]$ influences the numerical viscosity of the scheme. If $\theta = 1$, the scheme degenerates to the original minmod limiter, resulting in significant viscosity. Conversely, if $\theta = 2$, the scheme exhibits less viscosity and offers sharper resolution to shock waves. This reconstruction method is commonly referred to as the generalized minmod method.

Let us denote

$$\Delta^{\mathrm{CD}} q := \frac{q_3 - q_1}{2}$$

as the central difference approximation to the derivative of the solution. Based on the discussion in [33], the function (3.4) can be reformulated as

$$\mathrm{MM}_\theta(q_1, q_2, q_3) := \mathrm{sgn}(\Delta^{\mathrm{CD}} q) \min\big(|\Delta^{\mathrm{CD}} q|, \theta(q^{\max} - q_2), \theta(q_2 - q^{\min}) \big), \tag{3.5}$$

where

$$q^{\max} := \max(q_1, q_2, q_3), \quad q^{\min} := \min(q_1, q_2, q_3).$$

One immediate property of (3.5) is that

$$q^{\min} \le q_2 \pm \frac{1}{\theta} \cdot \mathrm{MM}_\theta q \le q^{\max}, \tag{3.6}$$

which can be extended as a IRP condition to general nonlinear systems.

In the Eq. (3.6), we used the sampled values provided by $\mathcal{L}_{\alpha,\beta}(\mathbf{x})$ at some points, which we refer to as extended interface midpoints, slightly away from the interface midpoints

$$\mathbb{I}^\theta_{\alpha,\beta} := \big\{ \mathbf{x}_{\alpha-\frac{1}{\theta},\beta}, \mathbf{x}_{\alpha+\frac{1}{\theta},\beta}, \mathbf{x}_{\alpha,\beta+\frac{1}{\theta}}, \mathbf{x}_{\alpha,\beta-\frac{1}{\theta}} \big\}. \tag{3.7}$$

When $\theta = 2$, these points coincide with the original interface midpoints $\mathbb{I}^{\theta=2}_{\alpha,\beta} = \mathbb{I}_{\alpha,\beta}$ (see Fig. 3.1).

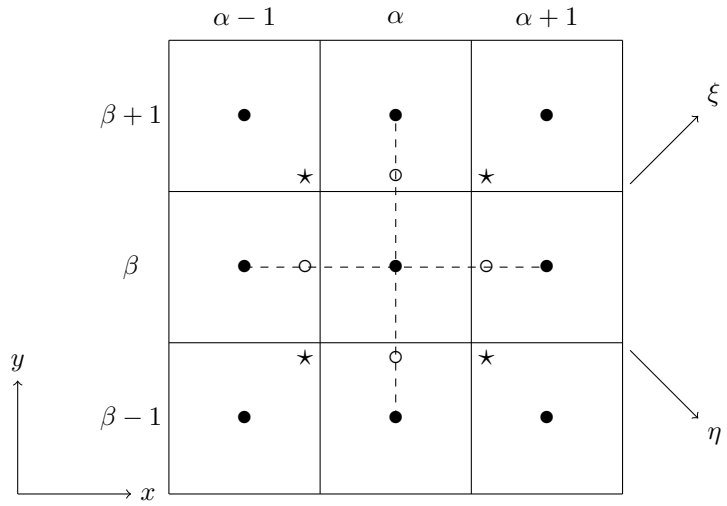

Fig. 3.1. IRP reconstructions in cell $C_{\alpha,\beta}$ at two different limiting points. Extended interface midpoints: $\circ$ (denoted as $\mathbb{I}^{\theta}_{\alpha,\beta}$ and becomes the interface midpoints when $\theta = 2$), Extended vertex points: $\star$ (denoted as $\mathbb{V}^{\theta}_{\alpha,\beta}$ and becomes the vertex points when $\theta = 2$).

Definition 3.1 (Interface Value Limiter). *A reconstruction is said extended interface value* IRP *if there exists a parameter* $\theta \in [1, 2]$ *such that*

$$\mathcal{L}_{\alpha,\beta}(\mathbf{x}) \in \Omega, \quad \forall\, \mathbf{x} \in \mathbb{I}^{\theta}_{\alpha,\beta}, \tag{3.8}$$

or equivalently

$$\mathbf{u}_{\alpha,\beta} \pm \frac{1}{\theta}\Delta\mathbf{u}_{\alpha,\beta} \in \Omega, \quad \Delta = \Delta_x \ \text{ or } \ \Delta_y \tag{3.9}$$

for any (α, β).

Remark 3.1. For any $\theta \in [1, 2]$ we have $(1/\theta) \in [1/2, 1]$. Thus (3.8)-(3.9) imply (2.11)-(2.12).

In existing literature [11, 20, 29, 30] the IVL method has been used for various applications. For scalar conservation laws, Jiang and Tadmor [11] derived the MMP CFL number

$$\mathrm{CFL}^{\mathrm{JT}}_{\theta} := \frac{\sqrt{4 + 6\theta - 3\theta^2} - 2}{6\theta}. \tag{3.10}$$

Compared with that in 1D case [24], these 2D CFL numbers are significantly smaller than half of the 1D value and present a degenerating problem

$$\lim_{\theta \to 2} \mathrm{CFL}^{\mathrm{JT}}_{\theta} = 0. \tag{3.11}$$

Similar problem happens if the trapezoidal method instead of the midpoint method to carry out the time integral in the evolution step [20]. For nonlinear hyperbolic systems, such as the nonlinear Euler equations, no stability results are obtained yet. The scheme is implemented following some linearization step. To illustrate the problem (3.11) we consider the following counter example.

Counter Example (Fig. 3.2). We will consider the linear advection equation

$$u_t - u_x - u_y = 0, \tag{3.12}$$

i.e. the fluxes takes the form, $f(u) = g(u) = -u$, with the initial condition

$$u^n_{i,j} = \begin{cases} 0, & \text{if} \quad i > I \quad \text{or} \quad j > J, \\ 1, & \text{if} \quad i = I \quad \text{and} \quad j = J, \\ 10, & \text{otherwise}, \end{cases} \tag{3.13}$$

where I and J are given integers. For this example, the minimum and maximum are $u^{\min} = 0$ and $u^{\max} = 10$, respectively.

Next, we compute the updated solution in cell $C_{I+1/2,\,J+1/2}$. We set $\theta = 2$ in the Eq. (3.4) for initial data reconstruction.

• First, let us consider the cells $C_{i,j}$ where (i, j) is either $(I{+}1, J), (I, J{+}1)$ or $(I{+}1, J{+}1)$. Using Eq. (3.3), the reconstruction yields $\Delta_x u^n_{i,j} = \Delta_y u^n_{i,j} = 0$, which results in

$$\mathcal{L}_{I+1,J+1}\big(\mathbf{x}_{I+\frac{3}{4},J+\frac{3}{4}}\big) = \mathcal{L}_{I+1,J}\big(\mathbf{x}_{I+\frac{3}{4},J}\big) = \mathcal{L}_{I,J+1}\big(\mathbf{x}_{I,J+\frac{3}{4}}\big) = 0.$$

Then the projected solution (2.6) takes the form

$$u_{I+\frac{1}{2},J+\frac{1}{2}} = \frac{1}{4}\mathcal{L}_{I,J}\big(\mathbf{x}_{I+\frac{1}{4},J+\frac{1}{4}}\big). \tag{3.14}$$

Using the reconstructed solution, we can obtain the predicted solutions and the corresponding fluxes

$$u^{n+\frac{1}{2}}_{i,j} = 0, \quad f\big(u^{n+\frac{1}{2}}_{i,j}\big) = g\big(u^{n+\frac{1}{2}}_{i,j}\big) = 0. \tag{3.15}$$

This gives us the residual

$$R_{I+\frac{1}{2},J+\frac{1}{2}} = \frac{f\big(u^{n+\frac{1}{2}}_{I,J}\big)}{2\Delta x} + \frac{g\big(u^{n+\frac{1}{2}}_{I,J}\big)}{2\Delta y} = -\left(\frac{1}{\Delta x} + \frac{1}{\Delta y}\right)\frac{u^{n+\frac{1}{2}}_{I,J}}{2}. \tag{3.16}$$

	$\cdots$	$I-1$	I	$I+1$	$\cdots$
$\vdots$	0	0	0	0	0
$J+1$	0	0	0	0	0
J	10	10	1	0	0
$J-1$	10	10	10	0	0
$\vdots$	10	10	10	0	0

Fig. 3.2. Counter example for initial data reconstruction.

Substituting Eqs. (3.14) and (3.16) into (2.9) gives us the updated solution in the dual cell $C_{I+1/2,J+1/2}$

$$u^{n+1}_{I+\frac{1}{2},J+\frac{1}{2}} = \frac{1}{4}\mathcal{L}_{I,J}\big(\mathbf{x}_{I+\frac{1}{4},J+\frac{1}{4}}\big) - \left(\frac{\Delta t}{\Delta x} + \frac{\Delta t}{\Delta y}\right)\frac{u^{n+\frac{1}{2}}_{I,J}}{2}, \tag{3.17}$$

which only depends on the interpolated solution at the projection point and the predicted solution in the cell $C_{I,J}$.

• Next, we consider the cell $C_{I,J}$. The reconstruction gives $\Delta_x u^n_{I,J} = \Delta_y u^n_{I,J} = -2$. Then the interpolated solution at the projection point becomes

$$\mathcal{L}_{I,J}\big(\mathbf{x}_{I+\frac{1}{4},J+\frac{1}{4}}\big) = 1 + \frac{1}{4}\left(\Delta_x u^n_{I,J} + \Delta_y u^n_{I,J}\right) = 0, \tag{3.18}$$

and the predicted solution at the cell center becomes

$$u^{n+\frac{1}{2}}_{I,J} = u^n_{I,J} + \frac{\Delta t}{\Delta x}\frac{\Delta_x u^n_{i,j}}{2} + \frac{\Delta t}{\Delta y}\frac{\Delta_y u^n_{i,j}}{2} = 1 - \left(\frac{\Delta t}{\Delta x} + \frac{\Delta t}{\Delta y}\right) > 0. \tag{3.19}$$

This holds true when the time step Δt is small enough due to the CFL condition. However the updated solution (3.17) is negative

$$u^{n+1}_{I+\frac{1}{2},J+\frac{1}{2}} < 0, \tag{3.20}$$

which means that the discrete minimum in the cell $C_{I+1/2,\,J+1/2}$ is violated.

The stability issues of the scheme can be understood through the above counter example. To avoid solving Riemann problems across the cell interfaces, the CS2D scheme computes the fluxes at the cell centers (2.10) and evolves the projected solutions in the dual cells (2.9). Prior to evolution, each primal cell is divided into four subcells and the mass of the conservative variables in each subcell is projected onto the corresponding dual cell. Ensuring that the cell center flux does not empty these four subcells is a challenge. Unfortunately, Eq. (3.18) in the counter example shows that the dual cell $C_{I+1/2,\,J+1/2}$ is already empty before evolution, thus nothing can flow out of this subcell.

3.2. Development of vertex value limiter

From the counter example, the main issue arises from the fact that the interpolated solution at the projection point is almost on the boundary of the invariant region

$$\mathcal{L}_{\alpha,\beta}\big(\mathbf{x}_{\alpha\pm\frac{1}{4},\beta\pm\frac{1}{4}}\big) \in \partial\Omega$$

even though the cell average is away from the boundary $\mathbf{u}_{\alpha,\beta} \in \Omega^o$. In this case we can see that the interpolated solution at the cell vertex is not physically meaningful

$$\mathcal{L}_{\alpha,\beta}\big(\mathbf{x}_{\alpha\pm\frac{1}{2},\beta\pm\frac{1}{2}}\big) \notin \Omega.$$

This motivates us to require that the reconstruction ensures that

$$\mathcal{L}_{\alpha,\beta}(\mathbf{x}) \in \Omega, \quad \forall\, \mathbf{x} \in \mathbb{V}_{\alpha,\beta} := \big\{\mathbf{x}_{\alpha-\frac{1}{2},\beta-\frac{1}{2}}, \mathbf{x}_{\alpha+\frac{1}{2},\beta-\frac{1}{2}}, \mathbf{x}_{\alpha-\frac{1}{2},\beta+\frac{1}{2}}, \mathbf{x}_{\alpha+\frac{1}{2},\beta+\frac{1}{2}}\big\}. \tag{3.21}$$

Similar to (3.7), we consider points, called extended vertex points, slightly away from the vertex points,

$$\mathbb{V}^{\theta}_{\alpha,\beta} := \big\{\mathbf{x}_{\alpha-\frac{1}{\theta},\beta-\frac{1}{\theta}}, \mathbf{x}_{\alpha+\frac{1}{\theta},\beta-\frac{1}{\theta}}, \mathbf{x}_{\alpha-\frac{1}{\theta},\beta+\frac{1}{\theta}}, \mathbf{x}_{\alpha+\frac{1}{\theta},\beta+\frac{1}{\theta}}\big\}. \tag{3.22}$$

When $\theta = 2$, the extended vertex points becomes the original vertex points $\mathbb{V}^{\theta=2}_{\alpha,\beta} = \mathbb{V}_{\alpha,\beta}$ (see Fig. 3.1).

Definition 3.2 (Vertex Value Limiter). *A reconstruction is said extended vertex value* IRP *if there exists a parameter* $\theta \in [1, 2]$ *such that*

$$\mathcal{L}_{\alpha,\beta}(\mathbf{x}) \in \Omega, \quad \forall\, \mathbf{x} \in \mathbb{V}^{\theta}_{\alpha,\beta}. \tag{3.23}$$

Remark 3.2. Notes that for any $\theta \in [1, 2]$, we have $(1/\theta) \in [1/2, 1]$. Thus (3.23) implies (3.21).

Remark 3.3. Another important point is that any point in $\mathbb{I}^{\theta}_{\alpha,\beta}$ is located at the centers of the line segment of two points in $\mathbb{V}^{\theta}_{\alpha,\beta}$. Thus a VVL method must also be a IVL method.

Direct calculation provides that

$$\mathcal{L}_{\alpha,\beta}\big(\mathbf{x}_{\alpha\pm\frac{1}{\theta},\beta\pm\frac{1}{\theta}}\big) = \mathbf{u}_{\alpha,\beta} + \frac{1}{\theta}\left(\pm\Delta_x\mathbf{u}_{\alpha,\beta} \pm \Delta_y\mathbf{u}_{\alpha,\beta}\right). \tag{3.24}$$

Let ξ denote the east-north direction and η denotes the east-south direction (see Fig. 3.1). We can define

$$\Delta_\xi\mathbf{u}_{\alpha,\beta} := \Delta_x\mathbf{u}_{\alpha,\beta} + \Delta_y\mathbf{u}_{\alpha,\beta}, \quad \Delta_\eta\mathbf{u}_{\alpha,\beta} := \Delta_x\mathbf{u}_{\alpha,\beta} - \Delta_y\mathbf{u}_{\alpha,\beta} \tag{3.25}$$

as the cell increments of solution between two pairs of vertex points along diagonal directions. Then the condition (3.23) can be rewritten as

$$\mathbf{u}_{\alpha,\beta} \pm \frac{1}{\theta}\Delta\mathbf{u}_{\alpha,\beta} \in \Omega, \quad \Delta = \Delta_\xi \text{ and } \Delta_\eta. \tag{3.26}$$

Conversely once $\Delta_\xi\mathbf{u}_{\alpha,\beta}$ and $\Delta_\eta\mathbf{u}_{\alpha,\beta}$ satisfying (3.26) are reconstructed, we use

$$\Delta_x\mathbf{u}_{\alpha,\beta} := \frac{1}{2}(\Delta_\xi\mathbf{u}_{\alpha,\beta} + \Delta_\eta\mathbf{u}_{\alpha,\beta}), \quad \Delta_y\mathbf{u}_{\alpha,\beta} := \frac{1}{2}(\Delta_\xi\mathbf{u}_{\alpha,\beta} - \Delta_\eta\mathbf{u}_{\alpha,\beta}) \tag{3.27}$$

to recover the gradient of the solution.

In the following sections, we will discuss the reconstruction of $\Delta_\xi\mathbf{u}_{\alpha,\beta}$ and $\Delta_\eta\mathbf{u}_{\alpha,\beta}$ for scalar problem and nonlinear Euler system, respectively.

3.2.1. Reconstruction for scalar problem

There are numerous methods for estimating $\Delta_\xi u_{\alpha,\beta}$ and $\Delta_\eta u_{\alpha,\beta}$ in a way that maintains the desired order of accuracy. For a rectangular mesh, the cell center $\mathbf{x}_{\alpha,\beta}$ is located centrally between two pairs of neighboring cell centers, i.e.

$$\mathbf{x}_{\alpha,\beta} = \frac{1}{2}(\mathbf{x}_{\alpha+1,\beta+1} + \mathbf{x}_{\alpha-1,\beta-1}) \quad \text{or} \quad \mathbf{x}_{\alpha,\beta} = \frac{1}{2}(\mathbf{x}_{\alpha+1,\beta-1} + \mathbf{x}_{\alpha-1,\beta+1}).$$

Furthermore the distance between two vertex points is half the distance between two neighboring cell centers

$$\begin{aligned}
\mathbf{x}_{\alpha+\frac{1}{2},\beta+\frac{1}{2}} - \mathbf{x}_{\alpha-\frac{1}{2},\beta-\frac{1}{2}} &= \frac{1}{2}(\mathbf{x}_{\alpha+1,\beta+1} - \mathbf{x}_{\alpha-1,\beta-1}),\\
\mathbf{x}_{\alpha+\frac{1}{2},\beta-\frac{1}{2}} - \mathbf{x}_{\alpha-\frac{1}{2},\beta+\frac{1}{2}} &= \frac{1}{2}(\mathbf{x}_{\alpha+1,\beta-1} - \mathbf{x}_{\alpha-1,\beta+1}).
\end{aligned}$$

Therefore, $\Delta_\xi u_{\alpha,\beta}$ and $\Delta_\eta u_{\alpha,\beta}$ can be simply estimated by the central difference method

$$\begin{aligned}
\Delta^{\mathrm{CD}}_\xi u_{\alpha,\beta} &:= \frac{1}{2}(u_{\alpha+1,\beta+1} - u_{\alpha-1,\beta-1}),\\
\Delta^{\mathrm{CD}}_\eta u_{\alpha,\beta} &:= \frac{1}{2}(u_{\alpha+1,\beta-1} - u_{\alpha-1,\beta+1}).
\end{aligned} \tag{3.28}$$

To control oscillation, similar to (3.5), we can establish

$$\Delta u_{\alpha,\beta} = \operatorname{sgn}\left(\Delta^{\mathrm{CD}} u_{\alpha,\beta}\right) \min\left(\left|\Delta^{\mathrm{CD}} u_{\alpha,\beta}\right|, \theta\left(u^{\max}_{\alpha,\beta} - u_{\alpha,\beta}\right), \theta\left(u_{\alpha,\beta} - u^{\min}_{\alpha,\beta}\right)\right) \tag{3.29}$$

for either Δ_ξ and Δ_η, where the local maximum and minimum are calculated among the neighboring cells

$$u^{\max}_{\alpha,\beta} := \max_{|i-\alpha|\le 1, |j-\beta|\le 1} u_{i,j}, \quad u^{\min}_{\alpha,\beta} := \min_{|i-\alpha|\le 1, |j-\beta|\le 1} u_{i,j}. \tag{3.30}$$

Following this reconstruction, it can be concluded that the local MMP principle is satisfied. It also adheres to the property (3.26), i.e. (3.23), and is therefore a VVL method.

Next, we will examine the performance of this new method in solving the counter example.

A revisit to the Counter Example (see Fig. 3.2). Considering $\theta = 2$ for the limiter in (3.29). It is clear that $\Delta_x u^n_{i,j} = \Delta_y u^n_{i,j} = 0$ for the cells $C_{I+1,J}$, $C_{I,J+1}$ or $C_{I+1,J+1}$. Thus, (3.17) still holds. We now focus on the cell $C_{I,J}$. Direct calculations show that $\Delta^{\mathrm{CD}}_\xi u_{I,J} = -5$, $\Delta^{\mathrm{CD}}_\eta u_{I,J} = 0$, and then, by (3.29) and (3.27)

$$\Delta_\xi u_{I,J} = -2, \quad \Delta_\eta u_{I,J} = 0, \quad \Delta_x u_{I,J} = \Delta_y u_{I,J} = -1. \tag{3.31}$$

Using the reconstructed state, we find the solution at the projection point

$$\mathcal{L}_{I,J}\left(\mathbf{x}_{I+\frac{1}{4},J+\frac{1}{4}}\right) = 1 + \frac{1}{4}\left(\Delta_x u^n_{I,J} + \Delta_y u^n_{I,J}\right) = \frac{1}{2}, \tag{3.32}$$

and the predicted solution at the cell center

$$u^{n+\frac{1}{2}}_{I,J} = u^n_{I,J} + \frac{\Delta t}{\Delta x}\frac{\Delta_x u^n_{i,j}}{2} + \frac{\Delta t}{\Delta y}\frac{\Delta_y u^n_{i,j}}{2} = 1 - \frac{1}{2}\left(\frac{\Delta t}{\Delta x} + \frac{\Delta t}{\Delta y}\right). \tag{3.33}$$

Substituting the above two equations into (3.17), the solution in the dual cell $C_{I+1/2,\,J+1/2}$ is updated

$$u^{n+1}_{I+\frac{1}{2},J+\frac{1}{2}} = \frac{1}{8} - \frac{1}{2}\left(\frac{\Delta t}{\Delta x} + \frac{\Delta t}{\Delta y}\right)\left(1 - \frac{1}{2}\left(\frac{\Delta t}{\Delta x} + \frac{\Delta t}{\Delta y}\right)\right), \tag{3.34}$$

which is lower bounded if the time step is small enough

$$\frac{1}{2}\left(\frac{\Delta t}{\Delta x} + \frac{\Delta t}{\Delta y}\right) < \frac{\sqrt{2}-1}{4} \implies u^{n+1}_{I+\frac{1}{2},J+\frac{1}{2}} > 0. \tag{3.35}$$

3.2.2. Reconstruction for nonlinear Euler equations

For a nonlinear system with conservative vector $\mathbf{u}$, we apply the method (3.29) to each component to control the oscillation. However, this approach is not inherently IRP. An additional limiter should be applied on the preliminary reconstructed $\Delta^{\#}\mathbf{u}_{\alpha,\beta}$ (Δ stands for Δ_ξ and Δ_η respectively) to satisfy the condition (3.23) or equivalently (3.26).

For the compressible Euler equations, which are in the conservative form (2.1) with

$$\mathbf{u} = \begin{pmatrix} \rho \\ \rho u \\ \rho v \\ E \end{pmatrix}, \quad \mathbf{f} = \begin{pmatrix} \rho u \\ \rho u^2 + p \\ \rho uv \\ u(E+p) \end{pmatrix}, \quad \mathbf{g} = \begin{pmatrix} \rho v \\ \rho vu \\ \rho v^2 + p \\ v(E+p) \end{pmatrix}, \tag{3.36}$$

where ρ is the gas density, $(u,v)^\top$ denotes the vertically averaged horizontal velocity, p represents the pressure, and

$$E=\frac{1}{2}\rho u^2+\frac{1}{2}\rho v^2+\frac{p}{\gamma-1}$$

describes the energy. The eigenvalues are $u-c,u,u,u+c$ of the Jacobian matrix $\mathbf{f}'_{\mathbf{u}}$ and $v-c,v,v,v+c$ of the Jacobian matrix $\mathbf{g}'_{\mathbf{u}}$ with the sound speed $c=\sqrt{\gamma p/\rho}$. Now the invariant domain is

$$\Omega=\{\mathbf{u}\mid \rho>0,\ p>0\}, \tag{3.37}$$

meaning that both density and pressure are positive. The IRP principle becomes the positivity-preserving principle. To realize the IRP property (3.26) we need

$$\rho_{\alpha,\beta}\pm\frac{1}{\theta}\Delta\rho_{\alpha,\beta}>0,\quad E_{\alpha,\beta}\pm\frac{1}{\theta}\Delta E_{\alpha,\beta}-\zeta^{\pm}>0, \tag{3.38}$$

where $\zeta^{\pm}$ are the interpolated kinetic energy

$$\zeta^{\pm}=\frac{\big((\rho u)_{\alpha,\beta}\pm\Delta(\rho u)_{\alpha,\beta}/\theta\big)^2}{2(\rho_{\alpha,\beta}\pm\Delta\rho_{\alpha,\beta}/\theta)}+\frac{\big((\rho v)_{\alpha,\beta}\pm\Delta(\rho v)_{\alpha,\beta}/\theta\big)^2}{2(\rho_{\alpha,\beta}\pm\Delta\rho_{\alpha,\beta}/\theta)}. \tag{3.39}$$

Following [27, 33], we perform the correction by

$$\begin{cases}\Delta\rho_{\alpha,\beta}=\operatorname{sgn}\big(\Delta^{\#}\rho_{\alpha,\beta}\big)\min\big(\theta\rho_{\alpha,\beta},\big|\Delta^{\#}\rho_{\alpha,\beta}\big|\big),\\ \Delta(\rho u)_{\alpha,\beta}=\max\big(u_{\alpha,\beta}\Delta\rho_{\alpha,\beta}-\varrho,\min\big(u_{\alpha,\beta}\Delta\rho_{\alpha,\beta}+\varrho,\Delta^{\#}(\rho u)_{\alpha,\beta}\big)\big),\\ \Delta(\rho v)_{\alpha,\beta}=\max\big(v_{\alpha,\beta}\Delta\rho_{\alpha,\beta}-\varrho,\min\big(v_{\alpha,\beta}\Delta\rho_{\alpha,\beta}+\varrho,\Delta^{\#}(\rho v)_{\alpha,\beta}\big)\big),\\ \Delta E_{\alpha,\beta}=\theta\max\Big(-E_{\alpha,\beta}+\zeta^{+},\min\big(E_{\alpha,\beta}-\zeta^{-},\frac{1}{\theta}\Delta^{\#}E_{\alpha,\beta}\big)\Big),\end{cases} \tag{3.40}$$

where ϱ and $\zeta^{\pm}$ are defined as follows:

$$\varrho=\theta\sqrt{\frac{\rho_{\alpha,\beta}p_{\alpha,\beta}}{\gamma-1}\left(1-\left(\frac{\Delta\rho_{\alpha,\beta}}{\theta\rho_{\alpha,\beta}}\right)^2\right)}. \tag{3.41}$$

Remark 3.4. Unlike the limiter in [36] for Euler equations, our limiter is explicitly defined and does not solve a quadratic equation. Furthermore, our limiter is applied only twice within a cell indicating a simpler and more efficient implementation.

4. Stability Analysis by Forward-backward Splitting Method

In this section, we conduct a thorough analysis of the scheme to establish its stability condition, leading to a suitable CFL number. The analysis employs the forward-backward splitting method, as introduced in [33]. Notably, this method is uniformly applicable to both scalar problems and nonlinear systems, accommodating both limiters: IVL and VVL.

Due to the convexity of the Ω, the IVL method (3.8) implies that

$$\mathcal{L}_{\alpha,\beta}\big(\mathbf{x}_{\alpha\pm\frac{1}{2\theta},\beta\pm\frac{1}{2\theta}}\big)=\frac{1}{2}\big(\mathcal{L}_{\alpha,\beta}\big(\mathbf{x}_{\alpha\pm\frac{1}{\theta},\beta}\big)+\mathcal{L}_{\alpha,\beta}\big(\mathbf{x}_{\alpha,\beta\pm\frac{1}{\theta}}\big)\big)\in\Omega.$$

On the other hand, the VVL method (3.23) implies that

$$\mathcal{L}_{\alpha,\beta}\big(\mathbf{x}_{\alpha\pm\frac{1}{\theta},\beta\pm\frac{1}{\theta}}\big)\in\Omega.$$

Therefore, for these two types of limiters, we have the following convex decomposition:

$$\mathcal{L}_{\alpha,\beta}\big(\mathbf{x}_{\alpha\pm\frac{1}{4},\beta\pm\frac{1}{4}}\big)=\tau\mathbf{u}_{\alpha,\beta}+(1-\tau)\boldsymbol{\mathcal{L}}_{\alpha,\beta}\big(\mathbf{x}^{\tau}_{\alpha\pm\frac{1}{4},\beta\pm\frac{1}{4}}\big), \tag{4.1}$$

where

$$\big(\tau,\mathbf{x}^{\tau}_{\alpha\pm\frac{1}{4},\beta\pm\frac{1}{4}}\big)=\begin{cases}\left(1-\dfrac{\theta}{2},\mathbf{x}_{\alpha\pm\frac{1}{2\theta},\beta\pm\frac{1}{2\theta}}\right), & \text{IVL},\\ \left(1-\dfrac{\theta}{4},\mathbf{x}_{\alpha\pm\frac{1}{\theta},\beta\pm\frac{1}{\theta}}\right), & \text{VVL}.\end{cases} \tag{4.2}$$

Given that $\theta\in[1,2]$, we can assert that $0<\tau<1$. A direct result is

$$\mathcal{L}_{\alpha,\beta}\big(\mathbf{x}_{\alpha\pm\frac{1}{4},\beta\pm\frac{1}{4}}\big)\in\Omega.$$

Based on (4.1) we give the following convex decomposition of the updated solution.

Lemma 4.1 (Forward-backward Decomposition). *Given an undetermine parameter $\kappa\in[0,\tau]$, the updated solution* (2.9) *in the dual cell at the new time level $t=t^{n+1}$ can be equivalently expressed as the following average:*

$$\mathbf{u}^{n+1}_{i+\frac{1}{2},j+\frac{1}{2}}=\kappa\mathbf{Q}^{n+\frac{1}{2}}_{i+\frac{1}{2},j+\frac{1}{2}}+\frac{\tau-\kappa}{4}\sum_{i'=0,1;\,j'=0,1}\mathbf{Q}_{i+i',j+j'}+(1-\tau)\mathbf{Q}^{\tau}_{i+\frac{1}{2},j+\frac{1}{2}}, \tag{4.3}$$

where

$$\begin{aligned}
\mathbf{Q}^{n+\frac{1}{2}}_{i+\frac{1}{2},j+\frac{1}{2}}&:=\frac{1}{4}\sum_{i'=0,1;\,j'=0,1}\mathbf{u}^{n+\frac{1}{2}}_{i+i',j+j'}+\frac{\Delta t}{\kappa}\cdot\mathbf{R}^{n+\frac{1}{2}}_{i+\frac{1}{2},j+\frac{1}{2}},\\
\mathbf{Q}_{i+i',j+j'}&:=\mathbf{u}^{n}_{i+i',j+j'}-\frac{\kappa}{\tau-\kappa}\frac{\Delta t}{2}\cdot\mathbf{R}^{n}_{i+i',j+j'},\qquad i'=0,1,\quad j'=0,1.\\
\mathbf{Q}^{\tau}_{i+\frac{1}{2},j+\frac{1}{2}}&:=\frac{1}{4}\sum_{i'=0,1;\,j'=0,1}\mathcal{L}_{i+i',j+j'}\Big(\mathbf{x}^{\tau}_{i+\frac{1}{4}+\frac{i'}{2},j+\frac{1}{4}+\frac{j'}{2}}\Big),
\end{aligned} \tag{4.4}$$

Proof. By utilizing the formula for $\mathbf{Q}^{n+1/2}_{i+1/2,j+1/2}$ we can express the updated solution (2.9) as follows:

$$\begin{aligned}
\mathbf{u}^{n+1}_{i+\frac{1}{2},j+\frac{1}{2}}=\kappa\mathbf{Q}^{n+\frac{1}{2}}_{i+\frac{1}{2},j+\frac{1}{2}}&+\frac{1}{4}\Big(\mathcal{L}_{i,j}\big(\mathbf{x}_{i+\frac{1}{4},j+\frac{1}{4}}\big)-\kappa\mathbf{u}^{n+\frac{1}{2}}_{i,j}\Big)+\frac{1}{4}\Big(\mathcal{L}_{i+1,j}\big(\mathbf{x}_{i+\frac{3}{4},j+\frac{1}{4}}\big)-\kappa\mathbf{u}^{n+\frac{1}{2}}_{i+1,j}\Big)\\
&+\frac{1}{4}\Big(\mathcal{L}_{i,j+1}\big(\mathbf{x}_{i+\frac{1}{4},j+\frac{3}{4}}\big)-\kappa\mathbf{u}^{n+\frac{1}{2}}_{i,j+1}\Big)+\frac{1}{4}\Big(\mathcal{L}_{i+1,j+1}\big(\mathbf{x}_{i+\frac{3}{4},j+\frac{3}{4}}\big)-\kappa\mathbf{u}^{n+\frac{1}{2}}_{i+1,j+1}\Big).
\end{aligned} \tag{4.5}$$

The convex decomposition (4.1) and the predicted solution (2.7) indicate that

$$\begin{aligned}
&\mathcal{L}_{i,j}\big(\mathbf{x}_{i+\frac{1}{4},j+\frac{1}{4}}\big)-\kappa\mathbf{u}^{n+\frac{1}{2}}_{i,j}\\
&=\tau\mathbf{u}^{n}_{i,j}+(1-\tau)\mathcal{L}_{i,j}\big(\mathbf{x}_{i+\frac{1}{4(1-\tau)},j+\frac{1}{4(1-\tau)}}\big)-\kappa\left(\mathbf{u}^{n}_{i,j}+\frac{\Delta t}{2}\mathbf{R}^{n}_{i,j}\right)\\
&=(\tau-\kappa)\left(\mathbf{u}^{n}_{i,j}-\frac{\kappa}{\tau-\kappa}\frac{\Delta t}{2}\mathbf{R}^{n}_{i,j}\right)+(1-\tau)\mathcal{L}_{i,j}\big(\mathbf{x}^{\tau}_{i+\frac{1}{4},j+\frac{1}{4}}\big)\\
&=(\tau-\kappa)\mathbf{Q}_{i,j}+(1-\tau)\mathcal{L}_{i,j}\big(\mathbf{x}^{\tau}_{i+\frac{1}{4},j+\frac{1}{4}}\big).
\end{aligned} \tag{4.6}$$

Similarly, we can derive that

$$\begin{aligned}
&\mathcal{L}_{i+1,j}\big(\mathbf{x}_{i+\frac{3}{4},j+\frac{1}{4}}\big) - \kappa \mathbf{u}_{i+1,j}^{n+\frac{1}{2}} = (\tau-\kappa)\mathbf{Q}_{i+1,j} + (1-\tau)\mathcal{L}_{i+1,j}\big(\mathbf{x}^{\tau}_{i+\frac{3}{4},j+\frac{1}{4}}\big),\\
&\mathcal{L}_{i,j+1}\big(\mathbf{x}_{i+\frac{1}{4},j+\frac{3}{4}}\big) - \kappa \mathbf{u}_{i,j+1}^{n+\frac{1}{2}} = (\tau-\kappa)\mathbf{Q}_{i,j+1} + (1-\tau)\mathcal{L}_{i,j+1}\big(\mathbf{x}^{\tau}_{i+\frac{1}{4},j+\frac{3}{4}}\big),\\
&\mathcal{L}_{i+1,j+1}\big(\mathbf{x}_{i+\frac{3}{4},j+\frac{3}{4}}\big) - \kappa \mathbf{u}_{i+1,j+1}^{n+\frac{1}{2}} = (\tau-\kappa)\mathbf{Q}_{i+1,j+1} + (1-\tau)\mathcal{L}_{i+1,j+1}\big(\mathbf{x}^{\tau}_{i+\frac{3}{4},j+\frac{3}{4}}\big).
\end{aligned} \tag{4.7}$$

By inserting the four aforementioned equations into (4.5), we obtain (4.3). This concludes the proof. □

Remark 4.1. In (4.4), the term $\mathbf{Q}^{n+1/2}_{i+1/2,\,j+1/2}$ can be interpreted as solving a forward process: $\mathbf{u}_t + \nabla\cdot\mathbf{f}(\mathbf{u}) = \mathbf{0}, \mathbf{Q}_{i+i',j+j'}$ corresponds to solving the backward process: $\mathbf{u}_t - \nabla\cdot\mathbf{f}(\mathbf{u}) = \mathbf{0}$, and $\mathbf{Q}^{\tau}_{i+1/2,j+1/2}$ derives its advantages from the property (4.1) of the initial data reconstruction.

The subsequent theorem outlines the condition for the stability of the 2D central scheme.

Theorem 4.1 (Stability Results). *If the time step satisfies*

$$\Delta t \cdot \max\left(\frac{\|\lambda(\mathbf{u})\|_\infty}{\Delta x}, \frac{\|\mu(\mathbf{u})\|_\infty}{\Delta y}\right) \le \frac{\sqrt{1+2\tau}-1}{4} =: \mathrm{CFL}, \tag{4.8}$$

where $\lambda(\mathbf{u})$ (respectively $\mu(\mathbf{u})$) is the spectral radius of the Jacobian matrix $\mathbf{f}_{\mathbf{u}}(\mathbf{u})$ (respectively $\mathbf{g}_{\mathbf{u}}(\mathbf{u})$), then $\mathbf{u}^{n+1}_{i+1/2,j+1/2}$ will be located within Ω.

Proof. The application of Lemma 4.1 and the convexity of the domain Ω means it is only necessary to establish the IRP property for $\mathbf{u}^{n+1/2}_{i,j}$, $\mathbf{Q}^{n+1/2}_{i+1/2,\,j+1/2}$ and $\mathbf{Q}_{i,j}$, respectively. Following this, the CFL number can be determined by appropriately selecting the parameter κ in (4.3).

(i) Estimation of $\mathbf{u}^{n+1/2}_{i,j}$. We take into account the predicted value computed by (2.7) at the half time step. Given the linearity of the reconstructed solution (2.4), it results in

$$\mathbf{u}^{n}_{i,j} = \frac{1}{4}\big(\mathcal{L}_{i,j}\big(\mathbf{x}_{i+\frac{1}{2},j}\big) + \mathcal{L}_{i,j}\big(\mathbf{x}_{i-\frac{1}{2},j}\big) + \mathcal{L}_{i,j}\big(\mathbf{x}_{i,j+\frac{1}{2}}\big) + \mathcal{L}_{i,j}\big(\mathbf{x}_{i,j-\frac{1}{2}}\big)\big). \tag{4.9}$$

This means that the predictor step (2.7) is in the form of the average of two staggered 1D Lax-Friedrichs schemes

$$\begin{aligned}
\mathbf{u}^{n+\frac{1}{2}}_{i,j} = {}& \frac{1}{2}\left(\frac{\mathcal{L}_{i,j}(\mathbf{x}_{i-1/2,j})+\mathcal{L}_{i,j}(\mathbf{x}_{i+1/2,j})}{2} - \frac{\Delta t}{\Delta x}\Big(\mathbf{f}\big(\mathcal{L}_{i,j}\big(\mathbf{x}_{i+\frac{1}{2},j}\big)\big) - \mathbf{f}\big(\mathcal{L}_{i,j}\big(\mathbf{x}_{i-\frac{1}{2},j}\big)\big)\Big)\right)\\
&+ \frac{1}{2}\left(\frac{\mathcal{L}_{i,j}(\mathbf{x}_{i,j-1/2})+\mathcal{L}_{i,j}(\mathbf{x}_{i,j+1/2})}{2} - \frac{\Delta t}{\Delta y}\Big(\mathbf{g}\big(\mathcal{L}_{i,j}\big(\mathbf{x}_{i,j+\frac{1}{2}}\big)\big) - \mathbf{g}\big(\mathcal{L}_{i,j}\big(\mathbf{x}_{i,j-\frac{1}{2}}\big)\big)\Big)\right).
\end{aligned} \tag{4.10}$$

Given that τ falls within the range $[0,1]$, the CFL number, as per Eq. (4.8), is constrained by the CFL number 1/2 of the staggered 1D Lax-Friedrichs scheme. This can be represented as

$$\mathrm{CFL} \le \frac{\sqrt{3}-1}{4} < \frac{1}{2}. \tag{4.11}$$

This implies that $\mathbf{u}^{n+1/2}_{i,j} \in \Omega$.

(ii) Estimation of $\mathbf{Q}^{n+1/2}_{i+1/2,\,j+1/2}$. Performing direct calculations results in

$$\begin{aligned}\mathbf{Q}^{n+\frac{1}{2}}_{i+\frac{1}{2},j+\frac{1}{2}} &= \frac{1}{4}\Bigg(\frac{\mathbf{u}^{n+\frac{1}{2}}_{i,j}+\mathbf{u}^{n+\frac{1}{2}}_{i+1,j}}{2}-\frac{2\Delta t}{\kappa\Delta x}\Big(\mathbf{f}\big(\mathbf{u}^{n+\frac{1}{2}}_{i+1,j}\big)-\mathbf{f}\big(\mathbf{u}^{n+\frac{1}{2}}_{i,j}\big)\Big)\Bigg)\\ &+\frac{1}{4}\Bigg(\frac{\mathbf{u}^{n+\frac{1}{2}}_{i,j+1}+\mathbf{u}^{n+\frac{1}{2}}_{i+1,j+1}}{2}-\frac{2\Delta t}{\kappa\Delta x}\Big(\mathbf{f}\big(\mathbf{u}^{n+\frac{1}{2}}_{i+1,j+1}\big)-\mathbf{f}\big(\mathbf{u}^{n+\frac{1}{2}}_{i,j+1}\big)\Big)\Bigg)\\ &+\frac{1}{4}\Bigg(\frac{\mathbf{u}^{n+\frac{1}{2}}_{i,j}+\mathbf{u}^{n+\frac{1}{2}}_{i,j+1}}{2}-\frac{2\Delta t}{\kappa\Delta y}\Big(\mathbf{g}\big(\mathbf{u}^{n+\frac{1}{2}}_{i,j+1}\big)-\mathbf{g}\big(\mathbf{u}^{n+\frac{1}{2}}_{i,j}\big)\Big)\Bigg)\\ &+\frac{1}{4}\Bigg(\frac{\mathbf{u}^{n+\frac{1}{2}}_{i+1,j}+\mathbf{u}^{n+\frac{1}{2}}_{i+1,j+1}}{2}-\frac{2\Delta t}{\kappa\Delta y}\Big(\mathbf{g}\big(\mathbf{u}^{n+\frac{1}{2}}_{i+1,j+1}\big)-\mathbf{g}\big(\mathbf{u}^{n+\frac{1}{2}}_{i+1,j}\big)\Big)\Bigg).\end{aligned}\tag{4.12}$$

By applying the stability condition of the 1D Lax-Friedrichs scheme, we can assert that $\mathbf{Q}^{n+1/2}_{i+1/2,\,j+1/2}\in\Omega$ provided that the following condition is met:

$$\frac{2}{\kappa}\mathrm{CFL}\le\frac{1}{2}\iff \mathrm{CFL}\le\frac{\kappa}{4}.\tag{4.13}$$

(iii) Estimation of $\mathbf{Q}_{i,j}$. Following the same logic as in Eq. (4.10), we find that

$$\begin{aligned}\mathbf{Q}_{i,j} &= \frac{1}{2}\Bigg(\frac{\mathcal{L}_{i,j}\big(\mathbf{x}_{i-\frac{1}{2},j}\big)+\mathcal{L}_{i,j}\big(\mathbf{x}_{i+\frac{1}{2},j}\big)}{2}\\ &\qquad-\frac{\kappa}{\tau-\kappa}\frac{\Delta t}{\Delta x}\Big(\mathbf{f}\big(\mathcal{L}_{i,j}\big(\mathbf{x}_{i-\frac{1}{2},j}\big)\big)-\mathbf{f}\big(\mathcal{L}_{i,j}\big(\mathbf{x}_{i+\frac{1}{2},j}\big)\big)\Big)\Bigg)\\ &+\frac{1}{2}\Bigg(\frac{\mathcal{L}_{i,j}\big(\mathbf{x}_{i,j-\frac{1}{2}}\big)+\mathcal{L}_{i,j}\big(\mathbf{x}_{i,j+\frac{1}{2}}\big)}{2}\\ &\qquad-\frac{\kappa}{\tau-\kappa}\frac{\Delta t}{\Delta y}\Big(\mathbf{g}\big(\mathcal{L}_{i,j}\big(\mathbf{x}_{i,j-\frac{1}{2}}\big)\big)-\mathbf{g}\big(\mathcal{L}_{i,j}\big(\mathbf{u}_{i,j+\frac{1}{2}}\big)\big)\Big)\Bigg).\end{aligned}\tag{4.14}$$

By again employing the stability condition of the 1D Lax-Friedrichs scheme, we can determine that $\mathbf{Q}_{i,j}\in\Omega$ if the following condition is fulfilled:

$$\frac{\kappa}{\tau-\kappa}\mathrm{CFL}\le\frac{1}{2}\iff \mathrm{CFL}\le\frac{\tau-\kappa}{2\kappa}.\tag{4.15}$$

(iv) Estimation of the parameters κ and CFL. Let us equate the right-hand side of Eqs. (4.13) and (4.15)

$$\frac{\kappa}{4}=\frac{\tau-\kappa}{2\kappa}\iff \frac{1}{2}\kappa^2+\kappa-\tau=0.\tag{4.16}$$

The solution to the above equation within the interval $[0,1]$ is

$$\kappa=\sqrt{1+2\tau}-1.\tag{4.17}$$

Substituting κ into either (4.13) or (4.15) gives the CFL number (4.8).

Up to this point, it has been demonstrated that $\mathbf{Q}_{i,j}\in\Omega$ and $\mathbf{Q}^{n+1/2}_{i+1/2,\,j+1/2}\in\Omega$ if condition (4.8) is met. The fact that $\mathbf{Q}^{\tau}_{i+1/2,\,j+1/2}\in\Omega$ is a direct result of assumption (4.1) and the final equation in (4.4). Therefor, the updated solution $\mathbf{u}^{n+1}_{i+1/2,\,j+1/2}$ is a convex summation of three states in Ω, as shown in (4.3), which implies $\mathbf{u}^{n+1}_{i+1/2,\,j+1/2}\in\Omega$. This completes the proof. □

The CFL number (4.8) is derived by equating the two terms (4.13) and (4.15). However, the CFL number is related to the value of τ given by (4.2), which is determined by the initial data reconstruction.

Theorem 4.2. *If the* IVL *method is utilized for the initial data reconstruction, then the scheme is* IRP *with the* CFL *number*

$$\mathrm{CFL}_\theta^{\mathrm{IVL}} = \frac{\sqrt{3-\theta}-1}{4}. \tag{4.18}$$

Alternatively, if the VVL *method is employed for the initial data reconstruction, then the scheme is* IRP *with the* CFL *number*

$$\mathrm{CFL}_\theta^{\mathrm{VVL}} = \frac{\sqrt{3-\theta/2}-1}{4}. \tag{4.19}$$

Remark 4.2. We compare the different CFL numbers in Fig. 4.1.

- Due to the use of the IVL method, the number $\mathrm{CFL}_\theta^{\mathrm{IVL}}$ also has degenerating problem,

$$\lim_{\theta\to 2} \mathrm{CFL}_\theta^{\mathrm{IVL}} = 0. \tag{4.20}$$

Its value is very close with $\mathrm{CFL}_\theta^{\mathrm{JT}}$ (3.10) and we can check that

$$\lim_{\theta\to 2} \frac{\mathrm{CFL}_\theta^{\mathrm{JT}}}{\mathrm{CFL}_\theta^{\mathrm{IVL}}} = 1.$$

- The degenerating problem is resolved by the VVL method,

$$\mathrm{CFL}_{\theta=2}^{\mathrm{VVL}} = \frac{\sqrt{2}-1}{4}, \tag{4.21}$$

which aligns with the stable condition (3.35) for the counter example.

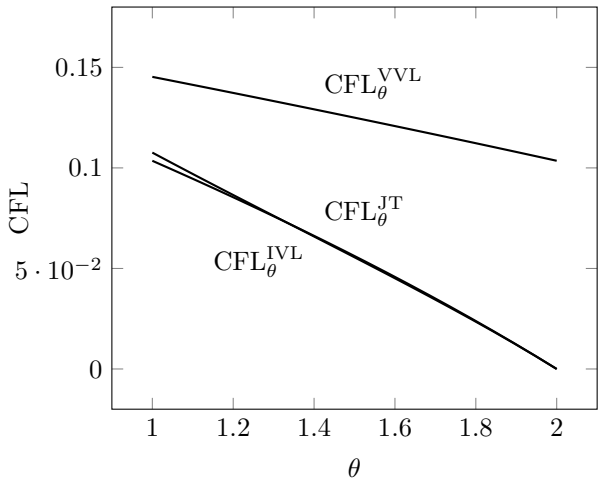

Fig. 4.1. Comparison of different CFL numbers. IVL: Interface value limiter, VVL: Vertex value limiter, JT: Method by Jiang and Tadmor [11].

• The number $\mathrm{CFL}_{\theta}^{\mathrm{VVL}}$ (4.19) is consistent with the one dimensional result in that it is equal to half the one dimensional number [33, 34].

Remark 4.3. The stability proof works not only for the scalar problems but also for the general nonlinear problems. Additionally, the proof is independent of the clipping condition used for the initial data reconstruction.

5. Numerical Experiments

In this section, we assess the numerical accuracy of the CS2D scheme enhanced with the VVL limiter. To validate its robustness, we compare it with the traditional IVL limiter, varying the parameter θ to 1 and 1.95, leading to different CFL numbers. The goal is to demonstrate the VVL's advantages. For clarity, we present the computed CFL numbers for both limiters

$$\mathrm{CFL}_{\theta=1}^{\mathrm{IVL}} \approx 0.1036, \quad \mathrm{CFL}_{1.95}^{\mathrm{IVL}} \approx 0.0062, \quad \mathrm{CFL}_{\theta=1}^{\mathrm{VVL}} \approx 0.1453, \quad \mathrm{CFL}_{1.95}^{\mathrm{VVL}} \approx 0.1058. \tag{5.1}$$

5.1. Scalar conservation laws

In this part, we examine the scheme by applying it to several scalar conservation laws. We verify the numerical accuracy for continuous problems and the maximum-minimum principle property through a discontinuous initial problem using a linear advection model. We also examine the resolution property of the two types of limiters in solving the 2D Buckley-Leverett equation.

Example 5.1. We consider the linear advection equation

$$u_t - u_x - u_y = 0 \tag{5.2}$$

with some initial condition $u(x, y, t = 0) = u_0(x, y)$. This type of simple model has the exact solution

$$u(x, y, t) = u_0(x + t, y + t), \tag{5.3}$$

if periodic or transverse boundary conditions are applied.

• We first test the accuracy by considering the smooth initial condition

$$u_0(x, y) = \sin\big(2\pi(x + y)\big) \tag{5.4}$$

on the domain $[0, 1] \times [0, 1]$ with the periodic boundary conditions [35]. The final time is $t = 0.1$. The numerical results of the L_1, L_2 and L_∞ errors by the VVL method with $\theta = 1.95$ are listed in Table 5.1 and the expected accuracy orders are achieved.

• Secondly we check the MMP property of the scheme. We consider the discontinuous initial condition

$$u_0(x, y) = \begin{cases} 1, & \text{if} \quad x < 0 \quad \text{and} \quad y < 0, \\ -1, & \text{otherwise} \end{cases} \tag{5.5}$$

with transverse boundary conditions on the domain $[-1, 1] \times [-1, 1]$.

The numerical results at the final time $t = 0.1$ are presented in Table 5.2. The first column represents the cell numbers. The second and third columns successfully demonstrate the MMP

Table 5.1: Example 5.1: Error and experimental order of convergence (EOC) for the linear advection equation (5.2) with continuous initial condition (5.4) with periodic boundary conditions. The final time is $t = 0.1$. The VVL method with $\theta = 1.95$ is used.

# cells	L_1 error	EOC	L_2 error	EOC	L_∞ error	EOC
50×50	1.415E-02	–	1.963E-02	–	4.858E-02	–
100×100	3.428E-03	2.05	5.550E-03	1.82	1.775E-02	1.45
200×200	7.717E-04	2.15	1.518E-03	1.870	6.200E-03	1.52
400×400	1.667E-04	2.21	4.047E-04	1.91	2.130E-03	1.54
800×800	3.527E-05	2.24	1.068E-04	1.92	7.300E-04	1.55

Table 5.2: Example 5.1: MMP property test for the advection equation (5.2) with discontinuous initial condition (5.5) at time $t = 0.1$. In this example, the maximum and minimum values are 1 and -1, respectively. Thus $1 - \max u \geq 0$ means that the maximum is maintained, $\min u + 1 \geq 0$ means that the minimum is maintained.

# cells	$\mathrm{CFL}^{\mathrm{VVL}}_{\theta=1.95} \approx 0.1058$		$\mathrm{CFL}^{\mathrm{IVL}}_{\theta=1.95} \approx 0.0062$		$1.1 \times \mathrm{CFL}^{\mathrm{IVL}}_{\theta=1.95} \approx 0.0068$	
	$1 - \max u$	$\min u + 1$	$1 - \max u$	$\min u + 1$	$1 - \max u$	$\min u + 1$
50×50	0.000E-00	0.000E-00	1.754E-13	0.000E-00	1.331E-13	-1.453E-10
100×100	0.000E-00	0.000E-00	8.882E-16	0.000E-00	8.882E-16	-8.738E-11
200×200	0.000E-00	0.000E-00	8.882E-16	0.000E-00	8.882E-16	-5.575E-11
400×400	0.000E-00	0.000E-00	1.332E-15	0.000E-00	8.882E-16	-3.705E-11
800×800	0.000E-00	0.000E-00	1.776E-15	0.000E-00	1.776E-15	-2.503E-11

property. However, the CFL number produced by the IVL method is excessively small. To address this, we increased the CFL number for IVL method by a factor of 1.1 and displayed the result in the last column. It is evident that, despite the enlargement, the CFL number remains very small compared to $\mathrm{CFL}^{\mathrm{VVL}}_{\theta=1.95}$, and as a consequence, the lower bound has been violated, specifically $\min u + 1 < 0$.

Example 5.2. We test the resolution to solve the 2D Buckley-Leverett equation with gravitational effects in the y-direction

$$f(u) = \frac{u^2}{u^2 + (1-u)^2}, \quad g(u) = \frac{u^2}{u^2 + (1-u)^2}\big(1 - 5(1-u)^2\big). \tag{5.6}$$

The initial data is

$$u_0(x, y) = \begin{cases} 1, & \text{if} \quad x^2 + y^2 < 0.5, \\ 0, & \text{otherwise} \end{cases} \tag{5.7}$$

on the domain $[-1.5, 1.5] \times [-1.5, 1.5]$ with transverse boundary conditions [8, 17]. The final time is $t = 0.5$. The major challenge of this problem is the nonconvex flux and the presence of a 2D composite wave structure in the solution.

The numerical outcomes pertaining to a 200×200 uniform grid are displayed in Fig. 5.1, which illustrate the robust stability of both IVL and VVL limiters. At $\theta = 1$, resolution drops due to high dissipation, as evident in the top two subfigures. At $\theta = 1.95$, an interesting phenomenon arises. For the IVL method, adherence to the CFL number defined in (5.1) leads to a diminished resolution, as shown in the lower left subfigure. While the VVL method

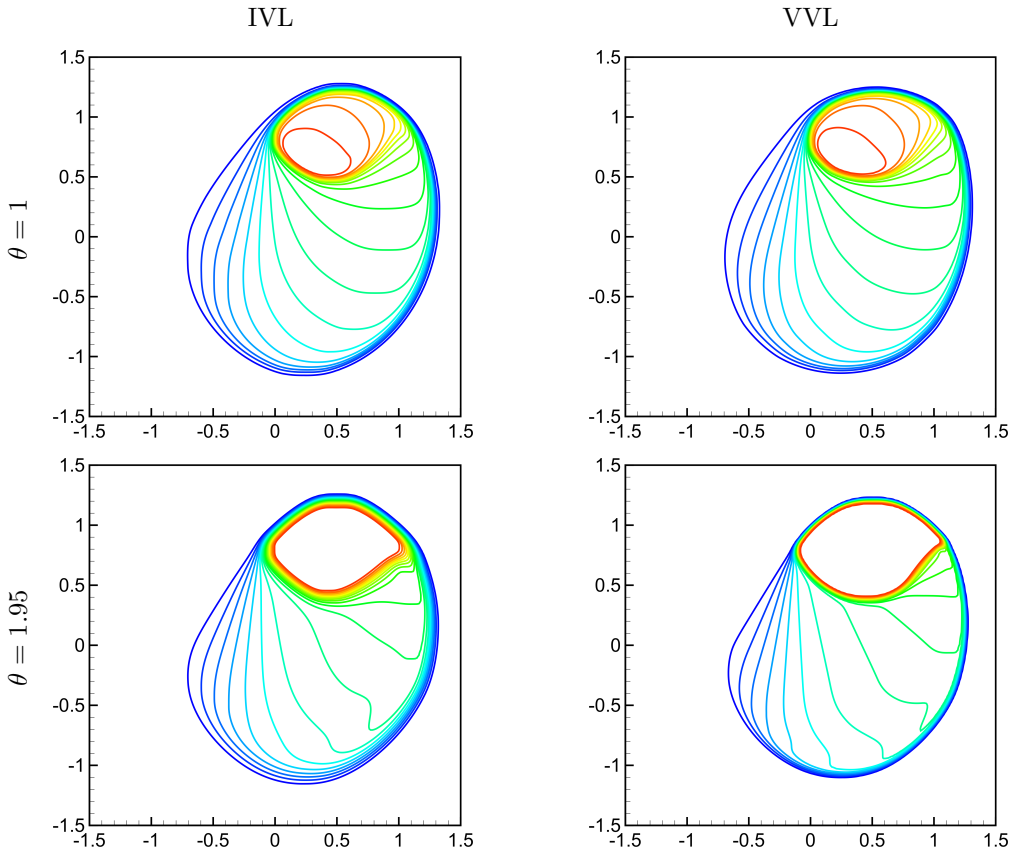

Fig. 5.1. Example 5.2: Buckley-Leverett problem. 19 contours in $[0.05, 0.95]$, $\Delta x = \Delta y = 0.015$.

demonstrates a marked enhancement in resolution, depicted in the lower right subfigure. This substantial improvement can be attributed to the VVL method's capability of achieving a higher CFL number, which permits larger time steps. Consequently, this strategy effectively mitigates numerical viscosity, leading to a more refined and accurate representation of the simulation outcomes.

5.2. Nonlinear Euler equations

In this part, we examine the proposed scheme by applying it to solve the compressible Euler equations (3.36). These include a low density problem, double Mach reflection problem, high Mach number astrophysical jets and shock reflection, and diffraction problem. Unless otherwise specified, $\gamma = 1.4$.

Example 5.3. Consider a low density problem using the initial data

$$\rho_0(x, y) = 1 + 0.99 \sin(x + y), \quad u_0(x, y) = v_0(x, y) = p_0(x, y) = 1 \tag{5.8}$$

on the domain $[0, 2\pi] \times [0, 2\pi]$ with the periodic boundary conditions [36]. The final time $t = 0.1$. The exact solution is

$$\rho(x, y, t) = 1 + 0.99 \sin(x + y - 2t), \quad u(x, y, t) = v(x, y, t) = p(x, y, t) = 1. \tag{5.9}$$

Table 5.3: Example 5.3: The low density problem. The numerical errors and experimental orders of convergence in different norms at time $t = 0.1$. The VVL method is used.

# cells	L_1 error	EOC	L_2 error	EOC	L_∞ error	EOC
50×50	0.285E-01	–	0.713E-02	–	0.521E-02	–
100×100	0.637E-02	2.16	0.178E-02	2.00	0.164E-02	1.67
200×200	0.130E-02	2.29	0.396E-03	2.17	0.461E-03	1.84
400×400	0.276E-03	2.24	0.895E-04	2.15	0.122E-03	1.92
800×800	0.635E-04	2.12	0.221E-04	2.02	0.383E-04	1.67

The accuracy results by the VVL method with $\theta = 1.95$ are listed in the Table 5.3. We clearly observe the designed order of the accuracy for this problem.

Example 5.4. We now solve the so-called double Mach reflection problem at Mach 10. This problem, first described by Woodward and Colella (see [31] for complete description), involves a Mach 10 shock in air hitting a wall at a 60° angle. The undisturbed air ahead of the shock has a density of 1.4 and a pressure of 1. The computational domain is $[0, 4] \times [0, 1]$. A reflection wall is placed at the bottom of the domain, starting from $x = 1/6, y = 0$, and it is parallel to the x-axis. The reflection boundary condition is applied at the wall, which for the rest of the bottom boundary (the part from $x = 0$ to $x = 1/6$), the exact postshock condition is imposed. At the top boundary, the exact motion of the Mach 10 shock is imposed. The results are displayed at time $t = 0.2$. We present pictures of the region $[0, 3] \times [0, 1]$, the blow-up region around the double Mach stems.

The numerical results for 960×240 uniform cells using different limiters with $\theta = 1.95$ are presented in Fig. 5.2. As evident in the figure, the VVL method exhibits significantly higher resolution compared to the IVL method scheme. Furthermore, a comparison of CPU time (Intel(R) Core(TM) i5-4590 CPU @ 3.30 GHz, serial computation, gfortran compiler) between the two different limiters reveals that the VVL method scheme required 67 h 52 m 26 s

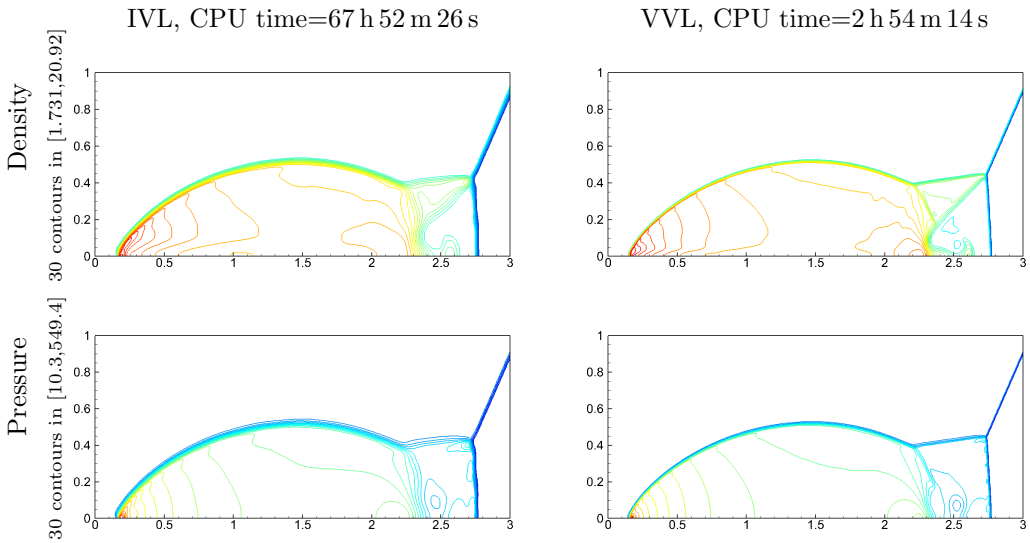

Fig. 5.2. Example 5.4: The Double Mach reflection problem. $\theta = 1.95, \Delta x = \Delta y = 1/240$.

CPU time, while the IVL method took 2 h 54 m 14s CPU time, corresponding to a simulation time 23.37 times longer. The results underscore that the VVL method, owing to its ability to attain a significantly higher CFL number as defined in (5.1), enables simulations to run considerably faster. This highlights the efficiency advantage of the VVL approach in accelerating the computational process.

Example 5.5. To address the problem at hand, we consider high Mach number astrophysical jets [27, 36]. We aim to compute a Mach 80 problem without radiative cooling. The computation domain is $[0, 2] \times [-0.5, 0.5]$ and is uniformly divided into 896×448 cells. Initially, the computational domain is filled with the ambient gas with $(\rho, u, v, p) = (0.5, 0, 0, 0.4127)$. For the boundaries, the right, top and bottom are set as outflow conditions. However, the left boundary condition is more complex. Specifically, for y within the range of $[-0.05, 0.05]$, the boundary conditions are $(\rho, u, v, p) = (5, 30, 0, 0.4127)$; otherwise, it is set as outflow. The terminal time for this problem is 0.07.

The high velocity of the gas introduces a risk of negative pressure, as the kinetic energy significantly surpasses the internal energy. Fig. 5.3 showcase stable simulations with both central schemes. Once again, the VVL method exhibits higher resolution and faster simulations. The VVL method produces satisfactory results when compared to existing literature, such as [6, 27, 36]. In contrast, the IVL method, with its higher viscosity, tends to blur the waves, rendering some small structures imperceptible. Notably, the VVL method (CPU time = 6 h 14 m 22 s) achieves significantly faster simulations than the IVL method (CPU time = 132 h 59 m 42 s).

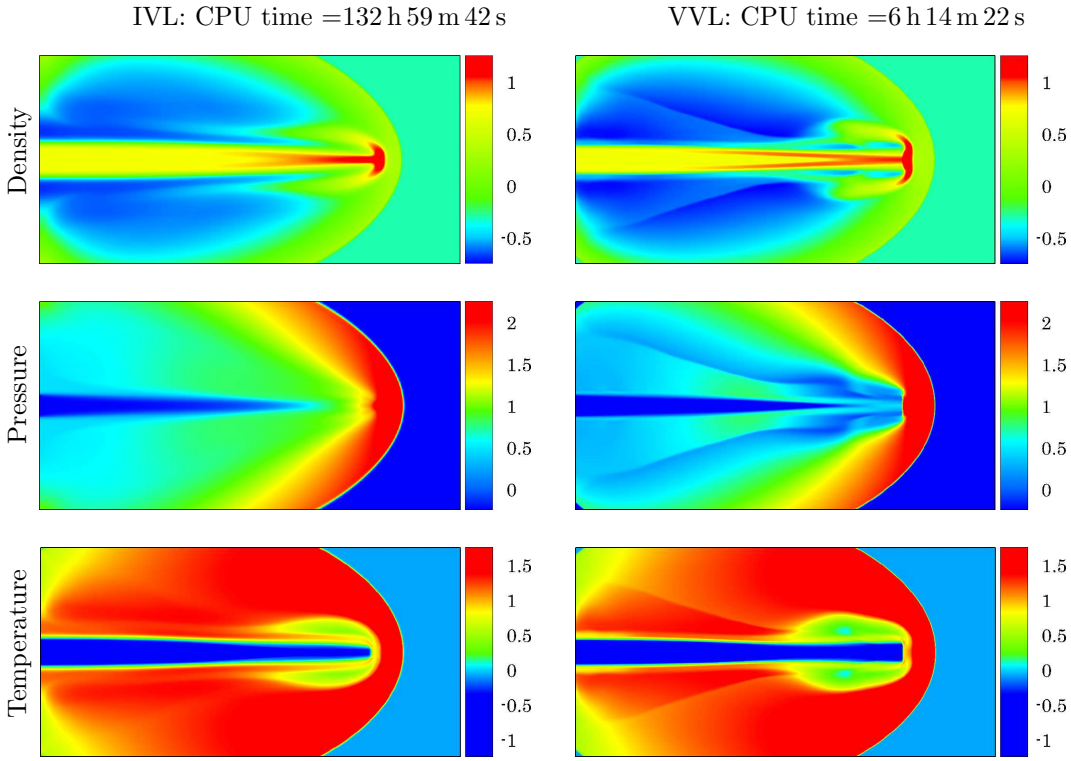

Fig. 5.3. Example 5.5: The Mach 80 astrophysical jets. $\theta = 1.95, \Delta x = \Delta y = 1/448$.

Example 5.6. Consider a Mach 10 shock reflection and diffraction problem [5, 6]. The computational domain is $[0,1]\times[0,1]$ and $[1,3]\times[-1,1]$. Initially a pure right-moving shock of Mach = 10 is positioned at $x = 1/6$, $y = 0$ and makes a 60° angle with a horizontal wall from $x = 1/6$ to 1. The undisturbed gas density ahead of the shock is $\rho = 1.4$, and the pressure is $p = 1$. Based on the Rankine-Hugoniot condition, the initial condition is

$$(\rho,u,v,p)=\begin{cases}(8.0,7.14471,-4.125,116.5), & \text{if} \quad y>\sqrt{3}(x-1/6), \quad y\geq 0,\\ (1.4,0,0,1), & \text{otherwise.}\end{cases} \tag{5.10}$$

The boundary conditions are set as follows: Inflow boundary condition is applied at the left edge $x = 0, 0 \le y \le 1$, the exact post-shock condition is posed at the boundary $0 \le x \le 1/6, y = 0$, reflective boundary condition is specified at the wall $1/6 \le x \le 1, y = 0$ and $x = 1, -1 \le y \le 0$, the top boundary is consistent with the exact motion of mach 10 shock, and outflow boundary condition is used at right and bottom edges. The terminal time is $t = 0.2$.

This test case intricately intertwines shock reflection and diffraction, encompassing a wide spectrum of phenomena including shocks, low-density regions, and low-pressure environments. Fig. 5.4 presents the initial density distribution alongside numerical outcomes, both obtained under a 1440×480 grid. Notably, the numerical results exhibit a commendable positivity-preserving characteristic.

When juxtaposed with the other two subfigures, the lower right subfigure stands out for its significantly superior resolution, highlighting a more refined portrayal of the dynamics. Furthermore, it underscores the capability of the VVL limiter to accommodate a broader range

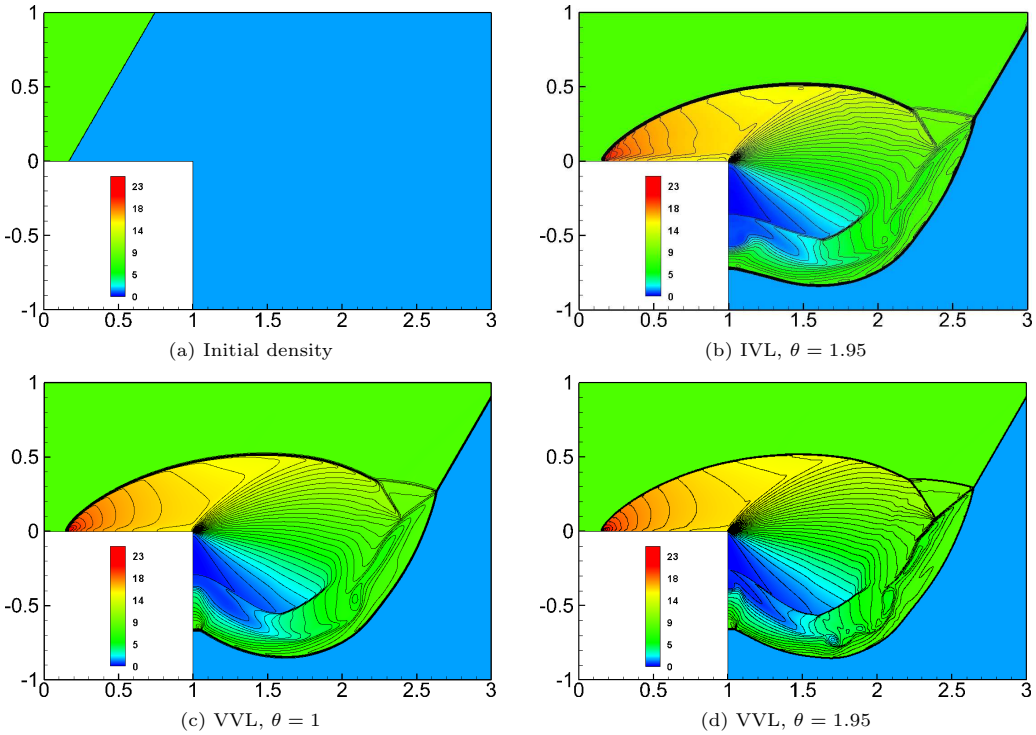

(a) Initial density (b) IVL, $\theta = 1.95$

(c) VVL, $\theta = 1$ (d) VVL, $\theta = 1.95$

Fig. 5.4. Example 5.6: Shock reflection and diffraction problem. 50 contours in $[0, 25]$ of density, $\Delta x = \Delta y = 1/480$.

of parameters, notably a larger θ value, which in turn facilitates the adoption of a higher CFL number. This versatility underscores the robustness of the methodology in simulating these intricate and complex physical phenomena.

6. Conclusion

This paper has delved into a thorough examination of the robustness of the 2D central scheme, with a primary focus on addressing challenges associated with the small and occasionally degenerating CFL numbers observed in stability analyses of scalar conservation laws solutions. Through an in-depth investigation, we identified that the limitation stems from the interface value limiter used in the initial data reconstruction, which proved insufficient in preserving the invariant region of updated solutions.

To rectify this shortcoming, we introduced the vertex value limiter, a novel approach that resulted in a more suitable CFL number, halving the one-dimensional value. Our unified proof of stability, applicable to both the mentioned limiters, has provided a comprehensive understanding of the enhanced stability conditions brought about by the VVL method. This breakthrough allows for the utilization of larger time steps, ultimately leading to improved resolution and faster simulations.

The scope of our analysis extends beyond scalar conservation laws to encompass general conservation laws, including both scalar problems and nonlinear systems. Numerical examples presented in this paper serve as compelling evidence, validating our claims and effectively showcasing the robustness of the enhanced scheme. The VVL limiter plays the pivotal role to enhance the overall stability and performance of the CS2D scheme. This research contributes not only to the theoretical understanding of stability in numerical methods but also provides a practical and effective solution for simulations involving conservation laws.

Looking ahead, future endeavors might delve into applying the VVL limiter to more intricate problems and exploring potential optimizations to further elevate its performance.

Acknowledgements. This work was supported by the National Natural Science Foundation of China (Grant No. 11371023), by the Postdoctoral Fellowship Program of CPSF (Grant No. GZB20240293), and by the Natural Science Foundation of Hubei Province, China (Grant No. 2025AFB841).

References

[1] P. Arminjon, D. Stanescu, and M.C. Viallon, A two-dimensional finite volume extension of the Lax-Friedrichs and Nessyahu-Tadmor schemes for compressible flow, in: *A Collection of Technical Papers, Proceedings of the 6th International Symposium on Computational Fluid Dynamics*, **4** (1995), 7–14.

[2] P. Arminjon, M.C. Viallon, and A. Madrane, A finite volume extension of the Lax-Friedrichs and Nessyahu-Tadmor schemes for conservation laws on unstructured grids, *Int. J. Comput. Fluid Dyn.*, **9** (1997), 1–22.

[3] G. Chen and S. Noelle, A new hydrostatic reconstruction scheme based on subcell reconstructions, *SIAM J. Numer. Anal.*, **55**:2 (2017), 758–784.

[4] G. Chen and S. Noelle, A unified surface-gradient and hydrostatic reconstruction scheme for the shallow water equations, *J. Comput. Phys.*, **467** (2022), 111463.

[5] C. Fan, X. Zhang, and J. Qiu, Positivity-preserving high order finite difference WENO schemes for compressible Navier-Stokes equations, *J. Comput. Phys.*, **467** (2022), 111446.

[6] C. Fan, Z. Zhao, T. Xiong, and J. Qiu, A robust fifth order finite difference Hermite WENO scheme for compressible Euler equations, *Comput. Methods Appl. Mech. Engrg.*, **412** (2023), 116077.

[7] J.-L. Guermond, M. Nazarov, B. Popov, and I. Tomas, Second-order invariant domain preserving approximation of the Euler equations using convex limiting, *SIAM J. Sci. Comput.*, **40**:5 (2018), A3211–A3239.

[8] J.-L. Guermond, R. Pasquetti, and B. Popov, Entropy viscosity method for nonlinear conservation laws, *J. Comput. Phys.*, **230**:11 (2011), 4248–4267.

[9] J.-L. Guermond and B. Popov, Invariant domains and first-order continuous finite element approximation for hyperbolic systems, *SIAM J. Numer. Anal.*, **54**:4 (2016), 2466–2489.

[10] G.-S. Jiang, D. Levy, C.-T. Lin, S. Osher, and E. Tadmor, High-resolution nonoscillatory central schemes with nonstaggered grids for hyperbolic conservation laws, *SIAM J. Numer. Anal.*, **35**:6 (1998), 2147–2168.

[11] G.-S. Jiang and E. Tadmor, Nonoscillatory central schemes for multidimensional hyperbolic conservation laws, *SIAM J. Sci. Comput.*, **19**:6 (1998), 1892–1917.

[12] Y. Jiang and H. Liu, Invariant-region-preserving DG methods for multi-dimensional hyperbolic conservation law systems, with an application to compressible Euler equations, *J. Comput. Phys.*, **373** (2018), 385–409.

[13] Y. Jiang and H. Liu, An invariant-region-preserving limiter for DG schemes to isentropic Euler equations, *Numer. Methods Partial Differential Equations*, **35**:1 (2019), 5–33.

[14] R. Kupferman and E. Tadmor, A fast, high resolution, second-order central scheme for incompressible flows, *Proc. Natl. Acad. Sci. USA*, **94**:1 (1997), 4848–4852.

[15] A. Kurganov and G. Petrova, A third-order semi-discrete genuinely multidimensional central scheme for hyperbolic conservation laws and related problems, *Numer. Math.*, **88**:4 (2001), 683–729.

[16] A. Kurganov and E. Tadmor, New high-resolution central schemes for nonlinear conservation laws and convection-diffusion equations, *J. Comput. Phys.*, **160**:1 (2000), 241–282.

[17] D. Kuzmin and M.Q. de Luna, Algebraic entropy fixes and convex limiting for continuous finite element discretizations of scalar hyperbolic conservation laws, *Comput. Methods Appl. Mech. Engrg.*, **372** (2020), 113370.

[18] D. Levy and E. Tadmor, Non-oscillatory central schemes for the incompressible 2-D Euler equations, *Math. Res. Lett.*, **4**:3 (1997), 321–340.

[19] M. Li, F. Li, Z. Li, and L. Xu, Maximum-principle-satisfying and positivity-preserving high order central discontinuous Galerkin methods for hyperbolic conservation laws, *SIAM J. Sci. Comput.*, **38**:6 (2016), A3720–A3740.

[20] K.-A. Lie and S. Noelle, An improved quadrature rule for the flux-computation in staggered central difference schemes in multidimensions, *J. Comput. Phys.*, **18**:1 (2003), 69–81.

[21] X.-D. Liu and E. Tadmor, Third order nonoscillatory central scheme for hyperbolic conservation laws, *Numer. Math.*, **79**:3 (1998), 397–425.

[22] Y. Liu, Central schemes on overlapping cells, *J. Comput. Phys.*, **209**:1 (2005), 82–104.

[23] Y. Liu, C.-W. Shu, E. Tadmor, and M. Zhang, Central discontinuous Galerkin methods on overlapping cells with a nonoscillatory hierarchical reconstruction, *SIAM J. Numer. Anal.*, **45**:6 (2007), 2442–2467.

[24] H. Nessyahu and E. Tadmor, Non-oscillatory central differencing for hyperbolic conservation laws, *J. Comput. Phys.*, **87**:2 (1990), 408–463.

[25] B. Popov and Y. Hua, Invariant domain preserving central schemes for nonlinear hyperbolic systems, *Commun. Math. Sci.*, **19**:2 (2021), 529–556.

[26] R. Sanders and A. Weiser, High resolution staggered mesh approach for nonlinear hyperbolic systems of conservation laws, *J. Comput. Phys.*, **101**:2 (1992), 314–329.

[27] W. Tong, R. Yan, and G. Chen, On a class of robust bound-preserving MUSCL-Hancock schemes, *J. Comput. Phys.*, **474** (2023), 111805.

[28] R. Touma and P. Arminjon, Central finite volume schemes with constrained transport divergence treatment for three-dimensional ideal MHD, *J. Comput. Phys.*, **212**:2 (2006), 617–636.

[29] R. Touma and F. Kanbar, Well-balanced central schemes for two-dimensional systems of shallow water equations with wet and dry states, *Appl. Math. Model.*, **62** (2018), 728–750.

[30] R. Touma, U. Koley, and C. Klingenberg, Well-balanced unstaggered central schemes for the Euler equations with gravitation, *SIAM J. Sci. Comput.*, **38**:5 (2016), B773–B807.

[31] P. Woodward and P. Colella, The numerical simulation of two-dimensional fluid flow with strong shocks, *J. Comput. Phys.*, **54**:1 (1984), 115–173.

[32] K. Wu, Minimum principle on specific entropy and high-order accurate invariant-region-preserving numerical methods for relativistic hydrodynamics, *SIAM J. Sci. Comput.*, **43**:6 (2021), B1164–B1197.

[33] R. Yan, W. Tong, and G. Chen, An efficient invariant-region-preserving central scheme for hyperbolic conservation laws, *Appl. Math. Comput.*, **436** (2023), 127500.

[34] R. Yan, W. Tong, and G. Chen, A mass conservative, well balanced and positivity-preserving central scheme for shallow water equations, *Appl. Math. Comput.*, **443** (2023), 127778.

[35] X. Zhang and C.-W. Shu, On maximum-principle-satisfying high order schemes for scalar conservation laws, *J. Comput. Phys.*, **229**:9 (2010), 3091–3120.

[36] X. Zhang and C.-W. Shu, On positivity-preserving high order discontinuous Galerkin schemes for compressible Euler equations on rectangular meshes, *J. Comput. Phys.*, **229**:23 (2010), 8918–8934.

[37] X. Zhang and C.-W. Shu, Positivity-preserving high order finite difference WENO schemes for compressible Euler equations, *J. Comput. Phys.*, **231**:5 (2012), 2245–2258.